Draft version January 16, 2024
Typeset using LaTeX **twocolumn** style in AASTeX631

Reconnection along a separator in shock turbulence

Anonymous author(s)

(Dated: January 16, 2024)

ABSTRACT

Numerous structures conducive to magnetic reconnection are frequently observed in the turbulent regions at quasi-parallel shocks. In this work, we use a particle-in-cell simulation to study three-dimensional magnetic reconnection in shock turbulence. We identify and characterise magnetic null points, and focus on reconnection along the separator between them. We identify a reconnection region with strong parallel current, a finite parallel potential and counter-rotating electron flows. Electrons are shown to be accelerated by the parallel electric field before being scattered at the null.

1. INTRODUCTION

Numerous reconnecting current sheets have been observed at and downstream of the transition region at Earth's bow shock (Gingell et al. 2020; Wang et al. 2019; Phan et al. 2018; Stawarz et al. 2022). In the quasi-parallel regions, these are the result of reflected particles exciting ion-ion instabilities (Wang et al. 2019; Bessho et al. 2020; Gingell et al. 2023) leading to the formation of intense current sheets, and further secondary instabilities causing electron-scale structures to form.

Kinetic and hybrid simulations have been a useful tool in studying the formation of reconnection regions and their importance in these transition regions. Previous investigations (Bessho et al. 2022) have demonstrated how electrons are accelerated, with the trapping of electrons in islands being a key mechanism, while Gingell et al. (2023) has studied a wide range of parameters to determine which are favourable for reconnection at quasi-parallel shocks. Three dimensional simulations have shown that a wider range of reconnection regimes can be accessed (Ng et al. 2022) as the additional degree of freedom allows weak guide field reconnection and differently oriented reconnection planes.

The simulation studies listed above have focused on two-dimensional or quasi-two-dimensional reconnection regions. In these quasi-2D systems, the "out-of-plane" direction parallel to the current is treated as slowly varying, with instabilities allowing the development of 3D structure. Generalizations of magnetic reconnection to three-dimensional systems (Schindler et al. 1988) have linked a finite value of $U_\parallel = -\int E_\parallel ds$ integrated along a field line to global topology change. Three dimensional structures are expected in the solar corona, at the magnetopause and different regions of the magnetosphere (Li et al. (2021a) and references therein). Based on theoretical considerations, there are different forms of reconnection that can take place at magnetic nulls (Priest & Pontin 2009), or along magnetic separators (Parnell et al. 2010a; Stevenson & Parnell 2015). "Slippage" reconnection can also occur in sheared flux tubes (Kuniyoshi et al. 2021).

Though many of the studies of 3d reconnection are in the context of solar physics (e.g. Priest & Pontin (2009); Parnell et al. (2010a); Pontin & Wyper (2015); Cheng et al. (2023)) and take place at MHD scales, there have been recent simulations and observations that discuss kinetic scales. MMS has observed the evolution of a null in the flank of the magnetopause (Ekawati & Cai 2023), while reconstruction using the magnetic field data of Cluster has allowed the identification of magnetic nulls and separators including events in turbulent regions (Guo et al. 2022). Kinetic simulations have been used to study nulls in different environments, where it is shown that energy dissipation is stronger in regions close to spiral nulls (Olshevsky et al. 2016).

In this paper we study 3D reconnection using a kinetic simulation of a quasi-parallel shock. We focus on a single event where we analyze reconnection along a separator between two magnetic nulls. We compare the properties of the plasma in this region and relate it to prior studies of separator reconnection, and anaylse the acceleration of electrons in the reconnection region. We show that parallel acceleration can increase the electron energy by an amount comparable to the electron temperature, but is likely to be overshadowed by the acceleration of electrons trapped in flux ropes.

2. SIMULATION SETUP

We perform three-dimensional simulations of a quasi-parallel shock using the fully-kinetic particle-in-cell code

VPIC (Bowers et al. 2008b,a). The initial condition consists of a uniform plasma and electromagnetic fields, with $B_x = B_0 \cos\theta_{Bn}$, $B_y = B_0 \sin\theta_{Bn}$ and $E_z = V_{flow} B_0 \sin\theta_{Bn}$, where θ_{Bn} is the angle between the magnetic field and shock normal ($\hat{\mathbf{x}}$). The initial plasma moves in the negative x direction with velocity $-V_{flow}$. The lower x boundary uses conducting walls for fields and reflecting walls for particles, while plasma is injected and the z-component of the electric field is imposed at the upper x boundary with the initial field and flow values. The y and z boundaries are periodic. The simulation domain is $1500 \times 500 \times 200\ (d_e)^3$ covered by $3000 \times 1000 \times 400$ cells, and is initialized with 150 particles per species per cell. Physical parameters used in the simulation are $\omega_{pe}/\Omega_{ce} = 4$, $m_i/m_e = 100$, $\beta_e = \beta_i = \sqrt{2}$, $\theta_{Bn} = 20°$ and $M_A = 10$. Here ω_{pe} is the electron plasma frequency, Ω_{ce} the electron cyclotron frequency, β the ratio between thermal pressure and magnetic pressure for either species and $M_A = V_{flow}/v_A$ the Alfvén Mach number of the injected plasma. As the simulation develops, the shock front propagates from the lower x boundary in the positive x direction. Unless otherwise mentioned in the text, length scales in the paper are normalized to d_e, and velocities to c, and number densities to the initial upstream density. Aside from the smaller θ_{Bn}, the physical conditions are similar to Ng et al. (2022).

3. RESULTS

An overview of the simulation is shown in Figure 1. In the quasi-parallel shock geometry, the interaction between incident and reflected ions leads to the generation of electromagnetic waves in the foreshock. Consequently, numerous current sheets form in the transition region and downstream of the shock, as shown in Figure 1(a).

In Figure 1(b), a 1-dimensional cut of the electron density along x with $y = 86, z = 94$ is shown. At this time, the shock is undergoing reformation and a new shock front is forming around $x = 500$. For the analysis of magnetic topology, we focus on a specific $(120 d_e)^3$ volume in the simulation domain, centered at $(349, 86, 94)$. The x extent of this region is shaded in Figure 1.

The region of interest in this work is the magnetic topology around the null points shown in Figure 2. Here the nulls have been located using the trilinear interpolation method of Haynes & Parnell (2007), and their character has been determined by using the eigenvalues and eigenvectors of the matrix $M_{ij} = \frac{\partial B_i}{\partial x_j}$ at the null. These are not the only nulls in the volume, but the analysis is confined to this specific region due to how it illustrates reconnection and electron acceleration.

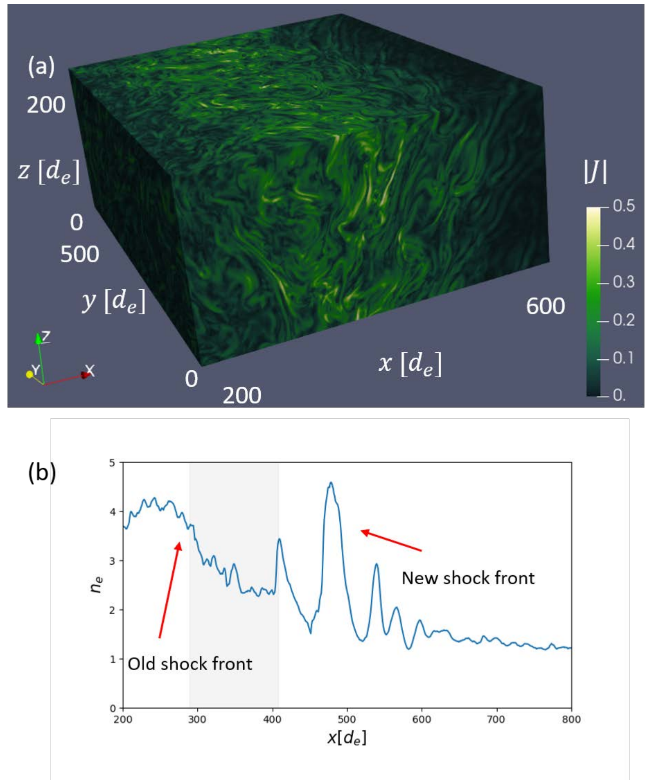

Figure 1. Overview of the shock simulation at $t\Omega_{ci} = 17$. The upstream region is to the right and plasma is flowing in the $-x$ direction. (a) Magnitude of the current density showing multiple current structures. (b) A cut at $y = 86, z = 94$ of the electron density showing the reforming shock. The shaded area illustrates the x extent of the volume used in the later figures.

In this figure the two null points are marked by spheres. The upper null (red) is a radial null with the matrix M_{ij} having three real eigenvalues, while the lower null (green) is a spiral null with M_{ij} having one real and two complex eigenvalues. The eigenvalues of the radial and spiral nulls are (0.17, -0.11, -0.066) and (0.042, -0.022+0.019i, -0.022-0.019i) respectively. The spiral structure is clearly visible in the fan plane of the lower null, while the straighter field lines associated with the radial null are clearest just below the upper null, though the changing magnetic field in the vicinity makes them challenging to see. At each null, the spine direction is shown by a white line. Field lines seeded in the vicinity of the upper null are shown in the darker pink, with the spine and fan planes marked by arrows, while the field topology around the lower null is shown by the lighter pink lines. The separator, which connects the two nulls, is shown by the thicker cyan line.

An analysis of the plasma parameters in this region is shown in Figure 3. In this figure, field lines are traced starting from the vicinity of the separator and shaded

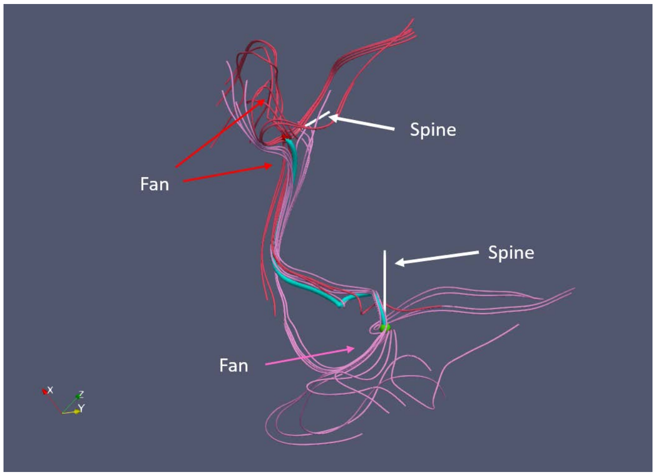

Figure 2. Topology around the null points in the quasi-parallel shock simulation. The nulls are marked by red and green spheres. Field lines showing the spine and fan for the upper and lower nulls are darker and lighter respectively. The separator is the thicker cyan line. The white lines show the direction of the spines at each null, and are $20d_e$ long. The total length along the separator is $98d_e$.

with different quantities. Particularly relevant to reconnection are the parallel electric field $E_\parallel$, parallel current $J_\parallel$, and the electron vorticity ω. Below the field line panels are $J_\parallel$ and $U_\parallel = -\int E_\parallel ds$ evaluated along the separator. Figure 3(a) shows that there is a region of intense parallel current just below the upper (red) null point. $E_\parallel$ in this region is highly nonuniform, which will be better quantified below. Towards the lower null point, the field lines are twisted and are beginning to form a flux rope where both $J_\parallel$ and $E_\parallel$ reverse sign.

The dynamics between the two nulls may be interpreted in terms of reconnection along a separator (Parnell et al. 2010a; Stevenson & Parnell 2015). As mentioned earlier, there are two regions with intense current density – the vertical region just below the red null towards the right, and the twisted region towards the left. Unlike the systems studied in Parnell et al. (2010a); Stevenson & Parnell (2015) where there are also multiple regions with an $E_\parallel$ signature, these regions have oppositely signed $E_\parallel$.

Similar to Parnell et al. (2010a,b); Stevenson & Parnell (2015); Hornig & Priest (2003), we compute the vorticity parallel to the magnetic field, which is shown in Figure 3(b). In this case, we use the electron vorticity rather than the ion vorticity based on $|\mathbf{E} + \mathbf{u}_e \times \mathbf{B}|$ being smaller than $|\mathbf{E} + \mathbf{u}_i \times \mathbf{B}|$ in the region of interest ($60 < s < 100$) as shown in Figure 3(h). The parallel component of the vorticity, $\omega_\parallel = (\nabla \times \mathbf{u}_e) \cdot \hat{\mathbf{b}}$, shows reversals, indicating the presence of counter-rotating flows which can cause the twisting of magnetic field lines.

A more detailed view of the electron flows is shown in Figure 4. Here two planes perpendicular to $\mathbf{B}$ corresponding to the local maximum and minimum of vorticity along the separator are shown. For each plane, the electron velocity is shown after subtracting the local bulk velocity, and in-plane streamlines are plotted. Using the local coordinate systems as defined in the Figure, the streamlines are shaded according to the x components of the velocity, while the planes are shaded according to the y components of the velocity. Viewing from above, the upper plane shows a clockwise rotation, while the lower plane shows an anti-clockwise rotation.

The parallel electron temperature and parallel electron velocity are also shown in Figure 3(e) and (f). Here, the parallel electron velocity is measured in the electron frame at the red null point. The region where the parallel velocity is large is consistent with the parallel current. On approaching the red null point, there is a reduction in the parallel velocity, with a corresponding increase in the parallel pressure. This is consistent with parallel momentum balance. The parallel temperature increases towards the end of the region with negative $J_\parallel$ close to the red null, but is reduced moving along the field lines past the null, suggesting that scattering is taking place.

In generalized magnetic reconnection, a finite value of the quantity $U_\parallel = -\int E_\parallel ds$ can be used to determine if reconnection has global consequences (Schindler et al. 1988). However, there is an assumption of an external ideal region, which is challenging to identify and may not exist in the turbulent environment. For completeness, we have evaluated this quantity, as shown in Figure 3(g). Large parallel potential variations can be seen in the $s < 20$ and $s > 50$ regions, where s is the distance along the field line, corresponding to the strong $E_\parallel$ in Figure 3(c).

In prior MHD studies of reconnection between two nulls (Parnell et al. 2010a,b), there are cases with multiple regions of enhanced reconnection along different parts of the separator, though the sign of $E_\parallel$ in these studies remains the same. As mentioned before, in Figure 3(c) and (g) there are two main regions where the potential variation is large ($s < 20$ and $s > 50$), with the parallel electric field being oppositely signed on average in these regions. We interpret this as two reconnection regions where the field lines are twisting in opposite directions.

In the rest of the paper, we focus on the vertical region with the strong negative parallel current just below the red null point. The average density and magnetic field in this region are 2.9 and 0.87 respectively, giving $Bv_A = 0.044$, while the average $E_\parallel$ is -0.003, giving $\langle E_\parallel \rangle / (Bv_A) \approx -0.06$. Interestingly, this is similar to

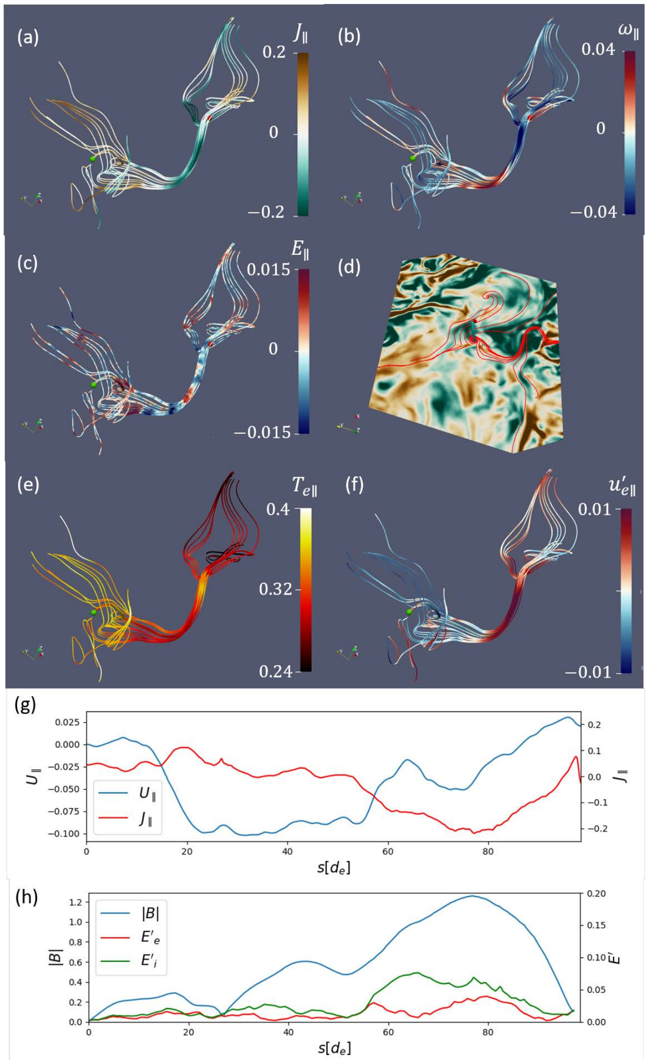

Figure 3. Field lines in the vicinity of the null points showing (a) $J_\parallel$, (b) $\omega_{e,\parallel}$ and (c) $E_\parallel$. (d) Parallel current density and magnetic field lines in a plane perpendicular to the separator (looking down from the right (red) null point) showing an O-point like structure. (e) Parallel electron temperature. (f) Parallel electron velocity in the electron frame at the right (red) null point. (g) Parallel current and parallel potential along the separator, starting from the left (green) null. (h) $|B|$ and $|E'$ where $\mathbf{E}'_s = \mathbf{E}_s + \mathbf{u}_s \times \mathbf{B}$.

the typical values in 2D and 3D reconnection sites with slow variation in the direction of the current (Birn et al. 2001; Cassak et al. 2017), though whether this is generally true requires further study.

Figure 3(d) shows the parallel current density and the in-plane structure of the magnetic field perpendicular to the separator. Here the field lines show an O-point like structure, which is a possibility during separator reconnection (Parnell et al. 2010a; Stevenson & Parnell 2015). This has implications for the detection of reconnection events which we will discuss later.

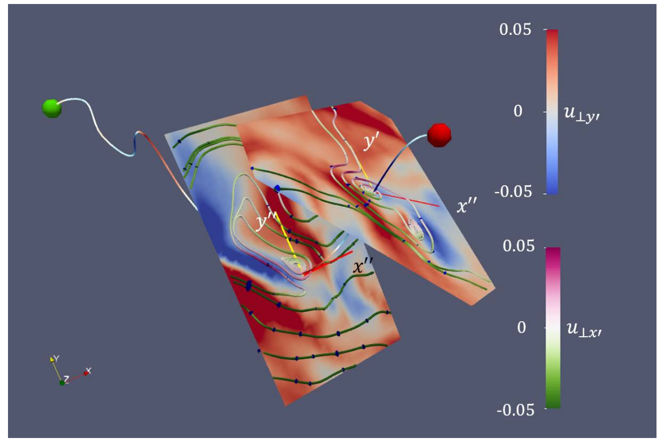

Figure 4. Rotating electron flows in planes perpendicular to the separator where the vorticity shows its local maximum and minimum. The colour scale for vorticity along the separator is the same as Figure 3(c). Electron velocities are calculated after subtracting the mean flow from $(6d_e)^3$ regions along the local maxima and minima. Red and yellow lines show local coordinate systems used to plot the in-plane velocity components. Streamlines are coloured by the x components, planes are coloured by the y components.

We now consider electron acceleration along the separator and close to the null, with a focus on the current layer. Figure 5 shows examples of trajectories of self-consistent tracer particles in this region. The shading of the trajectories indicates the simulation time, and the overplotted field lines use data from $t\Omega_{ci} = 17$, where the red and black parts of the trajectories meet. As such, the particles are in the region of strong $J_\parallel$ and mostly negative $E_\parallel$ during red parts of the trajectory, which takes place during the interval from $t\Omega_{ci} = 17$ to 17.125. The electrons travel towards the null, where they are scattered in different directions.

The work done by the parallel and total electric fields is shown in the lower panels, where $W = q\int \mathbf{E}\cdot\mathbf{v}_e dt$ and $W_\parallel = q\int E_\parallel v_\parallel dt$, shown by the blue and orange lines respectively. Initially, the acceleration is primarily due to the parallel electric field, after which the trajectories and acceleration mechanisms differ.

During the period between $t\Omega_{ci} = 17$ to $t\Omega_{ci} = 17.125$, the parallel energy gain of the particles is approximately $0.1 m_e c^2$, which is consistent with the maximum potential difference in Fig. 3. Particles do show acceleration before and after this interval, with #1 and #2 showing larger energy increases due to work done by the parallel electric field of approximately $0.25 m_e c^2$.

Because of the spatial and temporal scales of the system, the system is evolving throughout the period we analyze, while the parallel potential is calculated at a fixed time. Also, the particles do not travel along the separator for the entire duration. We investigate the

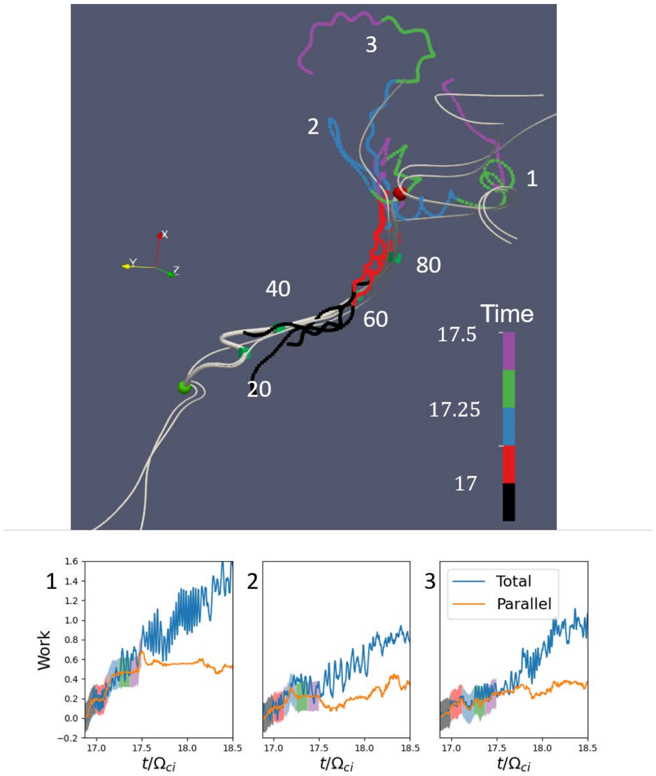

Figure 5. (Top) Particles accelerated along the separator with trajectories shaded by simulation time. The distances (s) corresponding to Figure 3 are marked by the boxes. (Bottom) Work done by total and parallel electric fields. Shading corresponds to the colors above representing time.

potential difference for nearby field lines at $t\Omega_{ci} = 17$ in Figure 6 understand its spatial variation. The field lines are seeded just after the twist in the separator close to the lower null. There are common features, such as the initial potential increase around $s = 20$, though the magnitude varies with position. At larger s, the field lines diverge, with the yellow line showing the largest potential difference of slightly less than $0.2 m_e c^2$. This is more consistent with the work done by the parallel electric field for particle #1 in particular, which travels towards the right (of the figure), close to this field line as it passes the null. Particles #2 and #3 initially travel towards the left of Figure 5 when close to the null (around $t\Omega_{ci} = 17.125$ when the trajectories transition from red to blue) where the field lines show a smaller potential difference, with both showing deceleration after being accelerated along the separator. Finally, it should also be re-emphasized that the field structure is drifting in the negative z, positive x direction (towards the left of the figure).

To evaluate the importance of the parallel acceleration, we focus on the trajectory of particle #1. Figure 7

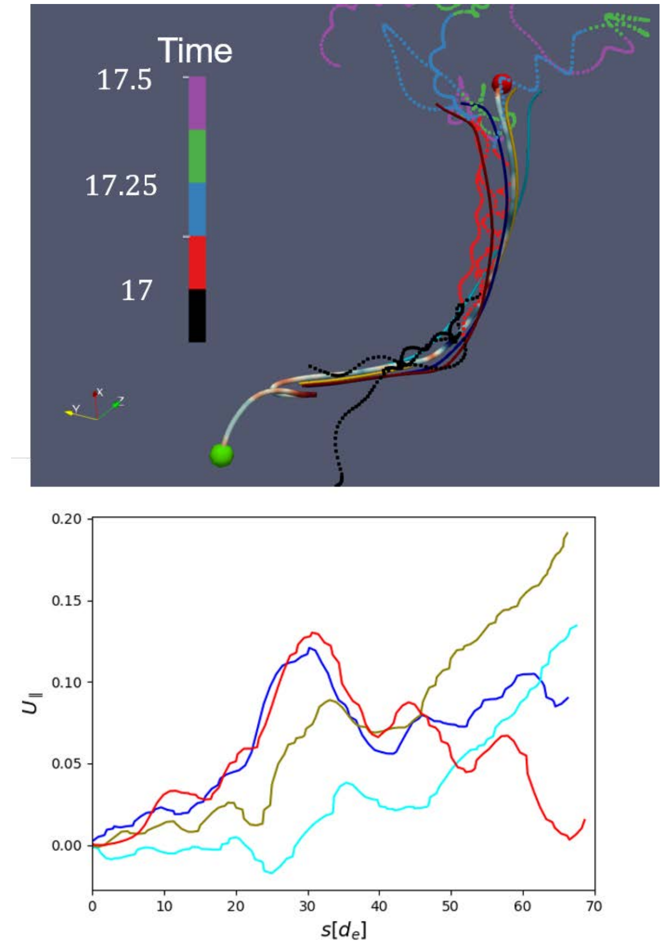

Figure 6. (Top) Field lines in the vicinity of the separator along with the sample electron trajectories. (Bottom) Integral of the parallel electric field along the field lines with colours corresponding to the field lines above.

shows the fate of this particle as it continues on its journey in the shock. There is further parallel acceleration as it moves past the null, followed by another jump in the work done due to both parallel and perpendicular acceleration at another reconnection site (shown in panel (a) at $t\Omega_{ci} = 17.5$). After this the particle enters a flux-rope like structure (panel (b) at $t\Omega_{ci} = 18$), where the work is primarily done by perpendicular electric fields, as can be seen in Figure 5, where the parallel work remains approximately constant after $t\Omega_{ci} = 17.5$. The energy increases at the second reconnection site and in the flux rope are larger than the increase close to the null, but are still of the same order of magnitude.

4. DISCUSSION AND SUMMARY

In this work we analyze 3D PIC simulation results of shock turbulence in the light of prior studies on separator reconnection. There are multiple differences between the configuration studied in this work and previous stud-

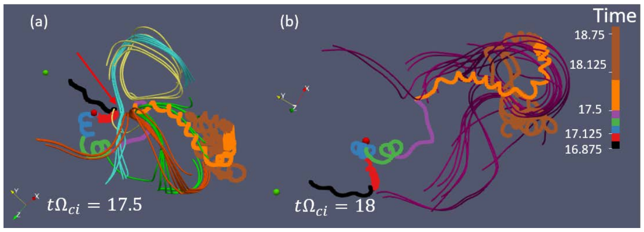

Figure 7. Extended trajectory of particle #1 showing field topology at (a) $t\Omega_{ci} = 17.5$ with a reconnection region marked by the arrow and (b) $t\Omega_{ci} = 18$ with a flux rope.

ies of separator reconnection. Many of these studies are at the MHD scale with a focus on solar flares (e.g. Priest & Pontin (2009); Parnell et al. (2010a); Stevenson & Parnell (2015); Parnell et al. (2010b); Threlfall et al. (2015)), and take place in idealised systems, while this work focuses on an event at kinetic scales within the shock transition region. Although the topological structures are the same, they are formed in a turbulent environment rather than from initial conditions constructed for the formation of nulls and separators which are then driven to reconnect. Nevertheless, it is still instructive to use these studies to help understand our results.

From the electron vorticity shown in Figure 3, the field topology changes are driven by counter-rotating plasma flows, similar to what is seen in Parnell et al. (2010a); Stevenson & Parnell (2015); Parnell et al. (2010b), though the field lines here follow the electron, rather than the ion flow. The presence of multiple actively reconnecting regions is similar to Parnell et al. (2010b), where there are multiple regions with strong $E_\parallel$. The small current and electric field at the null points suggests that reconnection is not taking place at these null points (Priest & Pontin 2009).

With respect to acceleration, Threlfall et al. (2015) used test particles to study electron acceleration along MHD-scale separator current layers, showing that electrons close to the reconnection regions are accelerated with most of the work done by the parallel electric field, similar to what is seen from the first part of the sample trajectories in Figure 5. The gain in energy depends on the parallel potential, which is controlled by the length scale of the reconnection regions and the parallel electric field. In the solar corona, this provides a means to accelerate electrons to high energies due to the large length scales involved ($\sim 10^6 m$ scale). In the fluctuating magnetosheath, it is difficult to provide an estimate of how large reconnection regions could be, but one expects correlation length scales of $\sim 10 d_i$ close to reconnection regions from statistical studies (Stawarz et al. 2022). For the event in this work, the reconnection region is approximately $5 d_i$ long. Because of the numerical parameters used in this simulation such as the reduced m_i/m_e and ω_{pe}/Ω_{ce}, the energy gain shown in the earlier analysis is larger than would be expected at the bow shock. If we assume $E_\parallel/(B v_A)$ remains the same, and use typical upstream values of $n_0 = 5$ cm^{-3}, $B_0 = 5$ nT for the solar wind at Earth (Russell 2001) and scaling B and n in the reconnection region appropriately, the energy gain would be $eE_\parallel L \approx 31$ eV, compared to the electron temperature of ≈ 18 eV using these parameters and $\beta_e = \sqrt{2}$. We may also consider more extreme upstream parameters such as those during solar flares (Tsurutani et al. 2006). For example, using $B_0 = 50$ nT and $n_0 = 15$ cm^{-3}, we find an energy gain of approximately 1 keV. Understanding the parameters for which this type of acceleration is significant will require further study.

Another difference between studies at MHD scales and kinetic scales is that the time scale of the electron transit along the separator is comparable to the time scale of the magnetic field evolution. This may contribute to the discrepancy between the potential difference and the energy gain, in addition to the spatial variation discussed earlier.

Other mechanisms of electron acceleration by reconnection in shocks have also been studied. In Bessho et al. (2023), it has been shown that electrons are accelerated at both electron-scale and ion-scale reconnection sites. During interactions with multiple electron-scale reconnection sites, the electrons are Fermi-reflected, but the most energetic electrons are those that are trapped in ion-scale magnetic islands. Both these mechanisms involve the perpendicular electric field, and the only significant parallel acceleration seen in that work is due to the pseudopotential across the shock. In this work the parallel electric field provides an additional mechanism for electron acceleration, with the energy gain comparable to the electron temperature. Trapping in a flux rope still provides a larger energy increase than the parallel acceleration, similar to the previous shock work (Bessho et al. 2022), or current sheet studies (Li et al. 2021b; Dahlin et al. 2017). Further work will be required to determine if the additional acceleration due to trapping in a moving island can still be achieved in three dimensions.

With respect to observations, this work is relevant to the quasi-parallel regions of Earth's bow shock. Current studies of reconnecting current sheets use various diagnostics to identify candidate events, including $|J|$, $\mathbf{B}$ reversals and electron flow perturbations (Gingell et al. 2020; Stawarz et al. 2022). Further analysis is then used to identify if these signatures are consistent with the reconnection geometry. However, in 3D reconnection, the magnetic topology may not have an X-point like structure in the 2D plane perpendicular to the separator (Parnell et al. 2010a,b; Stevenson & Parnell 2015). Figure 3(d) shows the magnetic field lines in a plane perpendicular to the separator within the reconnection region. Here the structure is more similar to an O-point, which may not be recognized by existing searches for reconnection which generally assume X-point like structures. Although magnetic nulls have been studied by in-situ measurements, their detection depends on accurate reconstruction of the magnetic field (Guo et al. 2022). Even when identifying strong $J_{\parallel}$, $E_{\parallel}$ and counter-rotating flows, it may be challenging to identify this form of reconnection if the null points are sufficiently far from the reconnection regions.

To summarise, we have identified three-dimensional reconnection along a separator in the quasi-parallel shock transition reigon. We have identified signatures such as $J_{\parallel}$, $E_{\parallel}$ and counter-rotating flows, which show similarities to separator reconnection studied at MHD scales. In the actively reconnecting region, electrons are accelerated by the parallel electric field, with the energy increase comparable to the work done by the reconnection electric field, before being scattered in different directions at the magnetic null. The work done by the parallel electric field is smaller than the later energy increase after trapping in a flux rope, and much smaller than the energy gain for electrons trapped in islands as seen in 2D simulations (Bessho et al. 2023). Finally, we have discussed how these results relate to MHD scale separator reconnection, and the potential of seeing this form of reconnection in observations such as that from NASA's Magnetospheric Multiscale mission.

(Acknowledgments anonymized for review)

REFERENCES

Bessho, N., Chen, L.-J., Hesse, M., et al. 2023, The Astrophysical Journal, 954, 25, doi: 10.3847/1538-4357/ace321

Bessho, N., Chen, L.-J., Stawarz, J. E., et al. 2022, Physics of Plasmas, 29, 042304, doi: 10.1063/5.0077529

Bessho, N., Chen, L.-J., Wang, S., et al. 2020, Physics of Plasmas, 27, 092901, doi: 10.1063/5.0012443

Birn, J., Drake, J. F., Shay, M. A., et al. 2001, Journal of Geophysical Research: Space Physics, 106, 3715, doi: 10.1029/1999JA900449

Bowers, K. J., Albright, B. J., Bergen, B., et al. 2008a, in Proceedings of the 2008 ACM/IEEE Conference on Supercomputing, SC '08 (Piscataway, NJ, USA: IEEE Press), 63:1–63:11. http://dl.acm.org/citation.cfm?id=1413370.1413435

Bowers, K. J., Albright, B. J., Yin, L., Bergen, B., & Kwan, T. J. T. 2008b, Physics of Plasmas, 15, 055703, doi: 10.1063/1.2840133

Cassak, P. A., Liu, Y.-H., & Shay, M. A. 2017, Journal of Plasma Physics, 83, 715830501, doi: 10.1017/S0022377817000666

Cheng, X., Priest, E. R., Li, H. T., et al. 2023, Nature Communications, 14, doi: 10.1038/s41467-023-37888-w

Dahlin, J. T., Drake, J. F., & Swisdak, M. 2017, Physics of Plasmas, 24, 092110, doi: 10.1063/1.4986211

Ekawati, S., & Cai, D. 2023, Journal of Geophysical Research: Space Physics, 128, doi: 10.1029/2021ja029571

Gingell, I., Schwartz, S., Kucharek, H., et al. 2023, Physics of Plasmas, 30, 012902

Gingell, I., Schwartz, S. J., Eastwood, J. P., et al. 2020, Journal of Geophysical Research: Space Physics, 125, e2019JA027119, doi: https://doi.org/10.1029/2019JA027119

Guo, R., Pu, Z., Wang, X., Xiao, C., & He, J. 2022, Journal of Geophysical Research: Space Physics, 127, doi: 10.1029/2021ja030248

Haynes, A. L., & Parnell, C. E. 2007, Physics of Plasmas, 14, 082107

Hornig, G., & Priest, E. 2003, Physics of Plasmas, 10, 2712, doi: 10.1063/1.1580120

Kuniyoshi, H., Hesse, M., Norgren, C., Tenfjord, P., & Kwagala, N. K. 2021, Journal of Geophysical Research: Space Physics, 126, doi: 10.1029/2021ja029236

Li, T., Priest, E., & Guo, R. 2021a, Proceedings of the Royal Society A, 477, 20200949

Li, X., Guo, F., & Liu, Y.-H. 2021b, Physics of Plasmas, 28, 052905, doi: 10.1063/5.0047644

Ng, J., Chen, L.-J., Bessho, N., et al. 2022, Geophysical Research Letters, 49, e2022GL099544, doi: https://doi.org/10.1029/2022GL099544

Olshevsky, V., Deca, J., Divin, A., et al. 2016, The Astrophysical Journal, 819, 52, doi: 10.3847/0004-637x/819/1/52

Parnell, C. E., Haynes, A. L., & Galsgaard, K. 2010a, Journal of Geophysical Research: Space Physics, 115, doi: https://doi.org/10.1029/2009JA014557

Parnell, C. E., Maclean, R. C., Haynes, A. L., & Galsgaard, K. 2010b, Proceedings of the International Astronomical Union, 6, 227, doi: 10.1017/s1743921311017650

Phan, T., Eastwood, J., Shay, M., et al. 2018, Nature, 557, 202

Pontin, D. I., & Wyper, P. F. 2015, The Astrophysical Journal, 805, 39, doi: 10.1088/0004-637x/805/1/39

Priest, E. R., & Pontin, D. I. 2009, Physics of Plasmas, 16, 122101, doi: 10.1063/1.3257901

Russell, C. T. 2001, Solar Wind and Interplanetary Magnetic Field: A Tutorial (American Geophysical Union (AGU)), 73–89, doi: https://doi.org/10.1029/GM125p0073

Schindler, K., Hesse, M., & Birn, J. 1988, Journal of Geophysical Research: Space Physics, 93, 5547, doi: https://doi.org/10.1029/JA093iA06p05547

Stawarz, J. E., Eastwood, J. P., Phan, T. D., et al. 2022, Physics of Plasmas, 29, 012302, doi: 10.1063/5.0071106

Stevenson, J. E. H., & Parnell, C. E. 2015, Journal of Geophysical Research: Space Physics, 120, 10,334, doi: 10.1002/2015ja021730

Threlfall, J., Stevenson, J. E. H., Parnell, C. E., & Neukirch, T. 2015, Astronomy & Astrophysics, 585, A95, doi: 10.1051/0004-6361/201527381

Tsurutani, B. T., Guarnieri, F. L., Fuller-Rowell, T., et al. 2006, Radio Science, 41, doi: https://doi.org/10.1029/2005RS003331

Wang, S., Chen, L.-J., Bessho, N., et al. 2019, Geophysical Research Letters, 46, 562, doi: https://doi.org/10.1029/2018GL080944